arXiv:1612.04909v2 [cond-mat.dis-nn] 7 Feb 2017

Deep Learning the Quantum Phase Transitions in Random Electron Systems: Applications to Three Dimensions

Tomi Ohtsuki[1*] and Tomoki Ohtsuki[2†]

[1]*Physics Division, Sophia University, Chiyoda-ku, Tokyo 102-8554, Japan*

[2] *NTT DATA Mathematical Systems Inc, Shinjuku-ku, Tokyo 160-0016, Japan*

Three-dimensional random electron systems undergo quantum phase transitions and show rich phase diagrams. Examples of the phases are band gap insulator, Anderson insulator, strong and weak topological insulators, Weyl semimetal, and diffusive metal. As in the previous paper on two-dimensional quantum phase transitions [J. Phys. Soc. Jpn. **85**, 123706 (2016)], we use image recognition algorithm based on multi-layered convolutional neural network to identify which phase the eigenfunction belongs to. Anderson model for localization-delocalization transition, Wilson-Dirac model for topological insulators, and layered Chern insulator model for Weyl semimetal are studied. The situation where the standard transfer matrix approach is not applicable is also treated by this method.

1. Introduction

Random three-dimensional (3D) electron systems show rich insulator and metal phases: band gap insulator, Anderson insulator,[1)] strong as well as weak topological insulator,[2,3)] Weyl semimetal,[4,5)] and diffusive metal are examples of the phases. The appearance of these phases[2,3,6,7)] is related to the basic symmetry such as time reversal, spin rotation, chiral, and particle-hole symmetries.[8–12)]

The eigenfunction of each phase exhibits specific features. In the Anderson insulator, the eigenfunctions are exponentially localized. Strong topological insulators (STI) exhibit two-dimensional (2D) Dirac electron on all the surfaces, while weak topological insulators (WTI) show 2D Dirac electron on specific surfaces determined by weak indices.[13)] In Weyl semimetal (WSM), surface states that form Fermi arc appear on surfaces parallel to the direction of split Weyl nodes.[14–16)]

In the presence of randomness, however, owing to the large amplitude fluctuations of

*ohtsuki@sophia.ac.jp
†ootsuki_t@msi.co.jp

eigenfunctions, determining the phases from eigenfunctions becomes difficult, especially when the system is close to phase boundaries. It is to be noted that topological numbers are usually defined in the randomness-free systems via the integration of the Berry curvature of Bloch function over the Brillouin zone. The definition is no longer valid once the randomness is introduced, which breaks the translational invariance. Hence new definition of topological numbers in random systems is necessary.[17–19)]

In the previous paper,[20)] we regarded the modulus squared (probability density) of an eigenfunction as an image, and used the image recognition[21)] based on deep learning[22,23)] to judge which phase the eigenfunction belongs to. Changing the stream of random numbers (MT2023) and their seeds, we have trained the convolutional neural network (CNN) by preparing large number of eigenfunctions belonging to each phase of random 2D electron systems, and have identified the phase of independently obtained eigenfunctions. The localization-delocalization transition in the presence of strong spin-orbit coupling (symplectic class),[24)] as well as Chern insulator-Anderson insulator transition (unitary class),[16,25)] has been verified.

In this paper, we further advance this approach to deal with 3D systems. 3D systems show even richer phases than 2D, such as strong and weak topological insulators and Weyl semimetals. We will first study the Anderson type 3D localization-delocalization transition. Then the phase diagrams of topological insulators are derived, followed by the demonstration of phase diagram for layered Chern insulator that exhibits Chern insulators (CI), WSM, and diffusive metal (DM) phases. We will demonstrate that the phase diagram can be obtained even in cases where the transfer matrix approach[26,27)] is not applicable.

2. Method

We adopt four-weight-layer convolutional neural network, which outputs real numbers $\in [0,1]$. Each number corresponds to the probability with which the input image belongs to certain phase. In the case of the Anderson transition, the output numbers are two, each corresponding to the probability of delocalized/localized phase. In the case of topological insulators, the output numbers are four, corresponding to ordinary insulator (OI), WTI, STI, and DM. The output numbers are three for layered Chern insulator, corresponding to CI, WSM, and DM.

We diagonalize 3D random electron systems on cubic lattice using sparse matrix diagonalization algorithm, Intel MKL/FEAST. We impose periodic boundary condition in y-direction, and integrate the modulus squared of the eigenfunction $\psi(x,y,z)$ to obtain the input

2D image $F(x,z)$,

$$F(x,z) = \int \mathrm{d}y\, |\psi(x,y,z)|^2 \,. \tag{1}$$

The lengths in the x- and z-directions are 40, so the input image is 40×40. The length in the y-direction is 40 for Anderson model and layered Chern insulator, 20 for topological insulator.

When we calculate the probability of delocalized/localized phase in the case of 3D Anderson transition, average over 5 samples are taken so that we can compare the 3D result with the case of 2D Anderson transition in the previous paper.[20] In the cases of topological insulator and layered Chern insulator, due mainly to the limitation of computational power, we do not take the sample average.

The four-weight-layer CNN used in this study is a variant of LeNet[28] included in Caffe[29] (with the input size changed to 40×40), which utilizes rectified linear unit (ReLU) as its activation function. The network weight parameters to be trained are sampled from Gaussian distribution of scale determined by the number of input and output dimensions,[30] except for the first convolution layer connected to the input image: in the first convolution layer, we have manually chosen the weight initialization scale to be 100. This choice of weight initialization scale is due to the fact that we deal with eigenfunctions, the values of which are typically much smaller than those of gray-scale images.

We have used the RMSProp solver[31] with the parameters in the Caffe MNIST example (which is contained as `examples/mnist/lenet_solver_rmsprop.prototxt` in the Caffe source) as the stochastic gradient descent solver. During the training, we randomly partition the training data set into 90% and 10%, and use the latter as the validation set. The solver performs enough iterations so that the validation error becomes stationary. Further details can be found in the previous paper.[20]

3. Applications to 3D Quantum Phase Transitions

3.1 Anderson transition

We first use the 3D Anderson model of localization, and discuss the Anderson transition.[1] The Hamiltonian is given by

$$H = \sum_{\boldsymbol{x}} v_{\boldsymbol{x}} c^\dagger_{\boldsymbol{x}} c_{\boldsymbol{x}} - \sum_{\langle \boldsymbol{x},\boldsymbol{x}' \rangle} c^\dagger_{\boldsymbol{x}} c_{\boldsymbol{x}'} \,, \tag{2}$$

where $c^\dagger_{\boldsymbol{x}}$ ($c_{\boldsymbol{x}}$) denotes the creation (annihilation) operator of an electron at a site $\boldsymbol{x} = (x,y,z)$, and $v_{\boldsymbol{x}}$ denotes the random potential at site $\boldsymbol{x}$. $\langle \cdots \rangle$ indicates the nearest neighbor hopping. We assume a box distribution with each $v_{\boldsymbol{x}}$ uniformly and independently distributed on the

interval $[-W/2, W/2]$. At energy $E = 0$, i.e., at the band center, the wave functions are delocalized when $W < W_c$ and the system is a diffusive metal. For $W > W_c$, the wave functions are localized and the system is an Anderson insulator (AI). The value of W_c is estimated to be around 16.54 by the transfer matrix method combined with the finite size scaling analyses.[32] We note here that multifractal finite size scaling analyses of wave functions reproduce the critical behavior of 3D Anderson model obtained by the transfer matrix method.[33,34]

As in the 2D symplectic case,[20] we prepared 1000 eigenfunctions in diffusive metal regime and 1000 eigenfunctions in Anderson insulator regime. We then prepared independent 100 eigenfunctions with various strength of disorder W, and let the machine judge whether they are delocalized (DM phase) or localized (AI phase). Results are shown in Fig. 1 (a), where the probabilities that the eigenfunction belongs to DM phase $P_{\rm DM}$ and to the AI phase $P_{\rm AI} = 1 - P_{\rm DM}$ are plotted as solid and dotted lines, respectively. Sharp transition from metal to insulator is observed near W_c.

As a test, we used the CNN trained for 2D DM–AI transition[20] to judge the 3D eigenfunctions. Results are plotted in Fig. 1 (b), where the transition is qualitatively captured, although the transition occurs earlier than it should.

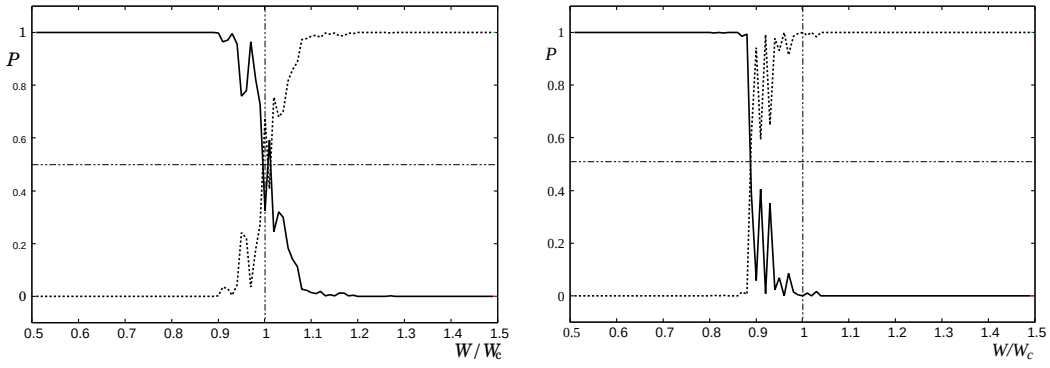

(a) (b)

Fig. 1. Probabilities that the eigenfunction near the band center belongs to the delocalized phase (solid line) and to the localized phase (dotted line). Average over 5 samples are taken. (a) Results of learning the 3D Anderson transition and (b) those of learning the 2D Anderson transition. Dashed dotted lines indicate 50% probability (horizontal line) and the critical disorder (vertical line).

3.2 3D topological insulators

We next study the phases of 3D topological insulators. We consider the following Wilson-Dirac type tight-binding Hamiltonian,[26,35]

$$H = \sum_{\boldsymbol{x}} \sum_{\mu=x,y,z} \left[\frac{it}{2} c^\dagger_{\boldsymbol{x}+\mathbf{e}_\mu} \alpha_\mu c_{\boldsymbol{x}} - \frac{m_{2,\mu}}{2} c^\dagger_{\boldsymbol{x}+\mathbf{e}_\mu} \beta c_{\boldsymbol{x}} + \text{H.c.} \right] + (m_0 + \sum_{\mu=x,y,z} m_{2,\mu}) \sum_{\boldsymbol{x}} c^\dagger_{\boldsymbol{x}} \beta c_{\boldsymbol{x}} + \sum_{\boldsymbol{x}} v_{\boldsymbol{x}} c^\dagger_{\boldsymbol{x}} 1_4 c_{\boldsymbol{x}}, \tag{3}$$

where $c^\dagger_{\boldsymbol{x}}$ and $c_{\boldsymbol{x}}$ are four-component creation and annihilation operators on a site $\boldsymbol{x}$, and $\mathbf{e}_\mu$ is a unit vector along μ-direction. α_μ and β are gamma matrices defined by

$$\alpha_\mu = \tau_x \otimes \sigma_\mu = \begin{pmatrix} 0 & \sigma_\mu \\ \sigma_\mu & 0 \end{pmatrix}, \ \beta = \tau_z \otimes 1_2 = \begin{pmatrix} 1_2 & 0 \\ 0 & -1_2 \end{pmatrix}, \tag{4}$$

where σ_μ and τ_μ are Pauli matrices that act on spin and orbital degrees of freedom, respectively. m_0 is the mass parameter, and $m_{2,\mu}$ and t are hopping parameters. Random potential $v_{\boldsymbol{x}}$ is uniformly and independently distributed between $[-W/2, W/2]$. We set $m_{2,x} = m_{2,y} = 1$ as energy unit. The Hamiltonian belongs to the symplectic class for $W > 0$. We impose fixed boundary conditions in x- and z-directions.

We first set $t = 2$ and $m_{2,z} = 0.5$. In this case, OI phase appears in $m_0 > 0$, STI phase in $0 > m_0 > -1$, WTI phase with weak index (001) in $-1 > m_0 > -2$, and WTI phase with weak index (111) in $-2 > m_0 > -3$.[36,37]

Let us first consider the features of surfaces states in the presence of small ramdomness. The situation is schematically described in Fig. 2. In the case of an STI or WTI(111), at $E \approx 0$, the surface states appear in x-y and y-z planes, but not in x-z plane, since we impose the periodic boundary condition in the y-direction. After integration over y, we expect amplitudes along the sides of x-z plane. On the other hand, the surface states at $E \approx 0$ appear only in the y-z planes for WTI(001), and the large amplitudes are expected along a z side. Whether they appear in the right z side or in the left depends on the configuration of random potential.

We set $W = 3.0$ and varied $m_0 \in [-1.8, -1]$ to teach the features of WTI(001), and $m_0 \in [-0.8, 0]$ to teach those of STI. These training parameters are along lines in W-m_0 plane, which are shown as dotted arrows in Fig. 3(a). To teach the features of DM, we set $W = 10.0$ and varied $m_0 \in [-2.5, 0.5]$, while for OI, we set $W = 3.0$ and varied $m_0 \in [0.2, 0.7]$. Actually, we do not know the phase diagram for the set of parameters we consider, so we assumed that changing $m_{2,z} = 1$ to 0.5 will not change the phase diagram drastically, and chose the parameters according to the knowledge of randomness-free case, $m_{2,z} = 0.5$ and $W = 0$,

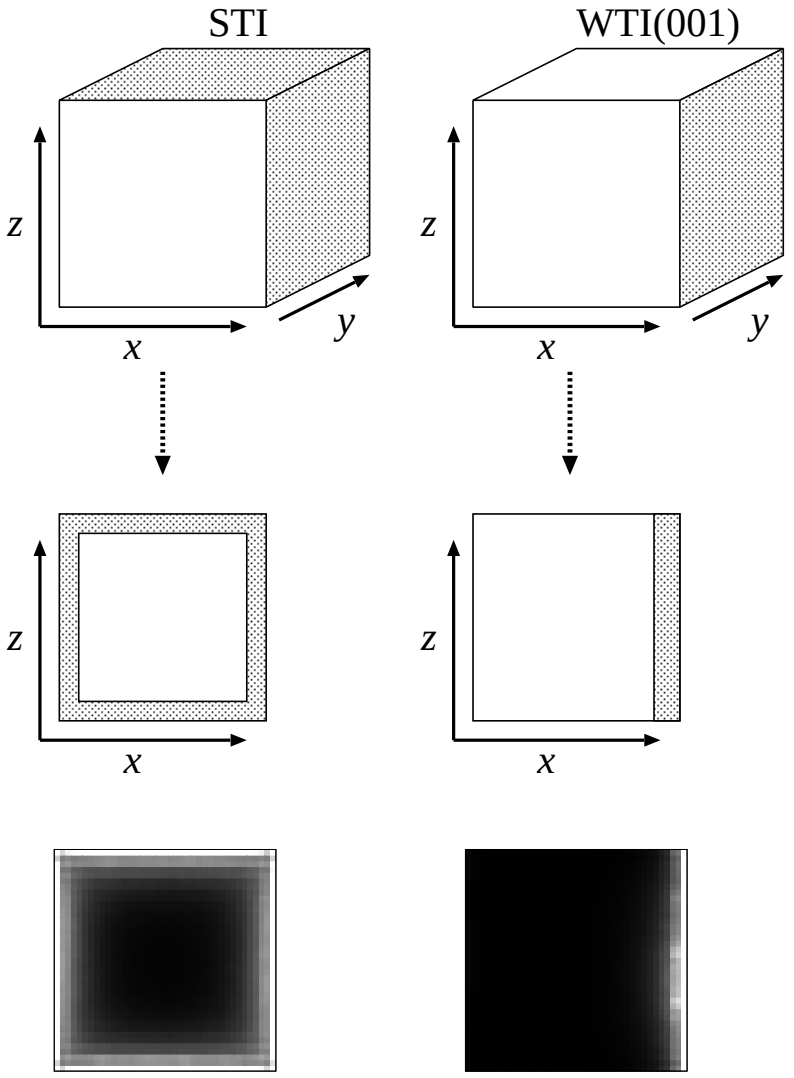

Fig. 2. Schematic of surface states in topological insulators, and the results of integration over y coordinate of numerically calculated eigenfunctions (bottom panels). Periodic boundary condition is imposed in y-direction, and fixed boundary condition in x- and z-directions. In the case of WTI(001), whether the strong amplitude region appears in the right ($x \approx 40$) or in the left ($x \approx 1$) depends on the specific configuration of randomness. In the bottom panels, the modulus squared of a numerically obtained eigenfunction integrated over y is shown. $(m_0, W) = (-0.16, 3)$ (STI, bottom left) and (-1.16, 3) [WTI(001), bottom right].

together with the information on the phase diagram for the isotropic but disordered case, $m_{2,z} = 1$ and $W > 0$.[27)]

After teaching 4000 eigenfunctions in each phase, we prepared new 100×27 eigenfunctions with different m_0 (100 values) and W (27 values), and let the machine judge which phase each eigenfunction belongs to. We calculate the probabilities $P_{\mathrm{OI}}, P_{\mathrm{W001}}, P_{\mathrm{SW111}}$, and

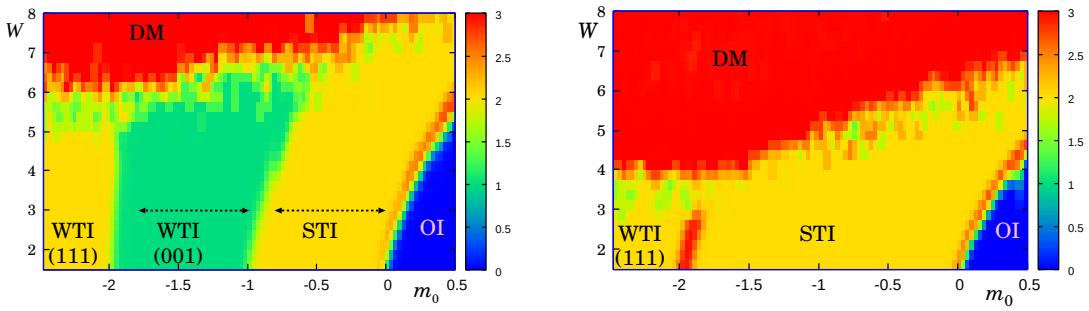

Fig. 3. Color map of $P_{\rm OI}, P_{\rm W001}, P_{\rm SW111}$, and $P_{\rm DM}$. The intensity $0 \times P_{\rm OI} + 1 \times P_{\rm W001} + 2 \times P_{\rm SW111} + 3 \times P_{\rm DM}$ is plotted. Shifts of the phase boundaries, OI/STI, STI/WTI(001), WTI(001)/WTI(111) by randomness is clearly seen. The arrows in (a) indicate the lines along which machine learning for STI and WTI(001) has been performed. The phase diagram where the transfer matrix method is not applicable, i.e., $t = m_{2,z} = 1$ is displayed in (b).

$P_{\rm DM}(= 1 - P_{\rm OI} - P_{\rm W001} - P_{\rm SW111})$ that a given eigenfunction belongs to OI, WTI(001), STI or WTI(111), and DM, respectively. Note that the present method cannot distinguish WTI(111) from STI, since WTI(111) contains surface states on all surfaces normal to x and z axes just as in STI, but from the knowledge of randomness-free case, we can reasonably determine whether the phase is STI or WTI(111).

The probabilities of OI, WTI(001), STI or WTI(111), and DM are displayed as a color map in the W-m_0 plane [Fig. 3 (a)]. We see that the phase boundaries between insulators with different topologies shift as we increase W. For example, when we start with OI phase, say $(m_0, W) = (0.3, 1.5)$ and increase disorder W, we enter into STI phase at $W \approx 6$. This is called the topological Anderson insulator (TAI) transition.[38–40] The present method captures TAI and gives a phase diagram quantitatively consistent with that obtained via the transfer matrix method.[27,41] It should be emphasized that one-dimensional training along a few finite lines in parameter space enables us to draw the 2D phase diagram.

We next apply the trained CNN of the above case, $t = 2$ and $m_{2,z} = 0.5$, to the case of $t = m_{2,z} = m_{2,x} = m_{2,y}(= m_2)$. In the absence of randomness, this choice of parameters gives OI for $m_0 > 0$, STI for $0 > m_0 > -2$, and WTI(111) for $-2 > m_0 > -4$.[36] The standard method of using the transfer matrix[27] to determine the phase diagram in the presence of disorder breaks down for this choice of parameters, since the transfer matrix connecting a layer to the next layer is not invertible for $t^2 - m_2^2 = 0$.[26] This choice of parameters, therefore, demonstrates the wider validity of the machine learning method. Results are shown in Fig. 3 (b).

Note that although the colors of STI and WTI(111) are the same, we can distinguish them by the emergence of the metal phase (in fact, it is Dirac semimetal phase[42]) sandwiched between insulators with different topology. Whether they are STI or WTI(111) can be determined from the randomness-free limit. Note also that the green region that appears on OI/STI boundary is not WTI(001) phase, but an artifact of the color map. See Appendix for detail.

3.3 Layered Chern insulator

We next consider two-dimensional Chern insulators,[16,25,43] and stack them in the z-direction to form three-dimensional Chern insulator and Weyl semimetal.[16,44] We begin with a spinless two-orbital tight-binding model on a square lattice, which consists of s-orbital and $p \equiv p_x + ip_y$ orbital,[45] and stack them in the z-direction to form cubic lattice,

$$\begin{aligned} H = &\sum_{\boldsymbol{x}} \Big((\epsilon_s + v_s(\boldsymbol{x})) c^\dagger_{\boldsymbol{x},s} c_{\boldsymbol{x},s} + (\epsilon_p + v_p(\boldsymbol{x})) c^\dagger_{\boldsymbol{x},p} c_{\boldsymbol{x},p} \Big) \\ &+ \sum_{\boldsymbol{x}} \Big(- \sum_{\mu=x,y} (t_s c^\dagger_{\boldsymbol{x}+\boldsymbol{e}_\mu,s} c_{\boldsymbol{x},s} - t_p c^\dagger_{\boldsymbol{x}+\boldsymbol{e}_\mu,p} c_{\boldsymbol{x},p}) \\ &\quad + t_{sp} (c^\dagger_{\boldsymbol{x}+\boldsymbol{e}_x,p} - c^\dagger_{\boldsymbol{x}-\boldsymbol{e}_x,p}) c_{\boldsymbol{x},s} - i t_{sp} (c^\dagger_{\boldsymbol{x}+\boldsymbol{e}_y,p} - c^\dagger_{\boldsymbol{x}-\boldsymbol{e}_y,p}) c_{\boldsymbol{x},s} + \text{H.c.} \Big) \\ &- \Big(t'_s c^\dagger_{\boldsymbol{x}+\boldsymbol{e}_z,s} c_{\boldsymbol{x},s} + t'_p c^\dagger_{\boldsymbol{x}+\boldsymbol{e}_z,p} c_{\boldsymbol{x},p} + \text{H.c.} \Big), \end{aligned}$$

where ϵ_s, $v_s(\boldsymbol{x})$, ϵ_p, and $v_p(\boldsymbol{x})$ denote atomic energy and disorder potential for the s- and p-orbitals, respectively. Both $v_s(\boldsymbol{x})$ and $v_p(\boldsymbol{x})$ are uniformly distributed within $[-W/2, W/2]$ with independent probability distribution. t_s, t_p, and t_{sp} are transfer integrals between neighboring s-orbitals, p-orbitals, and that between s- and p-orbitals, respectively. t'_s and t'_p are interlayer transfer integrals.

As in ref.[16] we set $\epsilon_s - \epsilon_p = -2(t_s + t_p)$, $t'_s = -t'_p > 0$, $t_s = t_p > 0$, and $t_{sp} = 4t_s/3$, and took $4t_s$ as the energy unit. In the absence of randomness, this set of parameters realizes a CI with a large band gap in the 2D limit, $\beta \equiv \frac{t'_p - t'_s}{2(t_s+t_p)} = 0$. As long as $1/2 > |\beta| \geq 0$, the system is fully gapped, and the system belongs to CI phase. The system enters into 3D WSM phase for $|\beta| > 1/2$.[16]

In the presence of randomness, there appear four phases: CI, WSM, DM and AI. AI phase appears in large W region. Here we focus on the first three phases by considering $W < 4.5$ and $0.3 < \beta < 0.6$. Note that there is a correspondence between CI and WTI, and WSM and STI.[44]

As in the previous subsection, let us first consider the features of states near $E = 0$ in the case of small randomness. The situation is schematically described in Fig. 4, where periodic

boundary conditions are imposed in y- and z-directions, while fixed boundary condition is imposed in x-direction. In the case of a CI, at $E \approx 0$, edge states run along y-direction, and after integration over y, we expect amplitudes in a dot in x-z plane close to a side along z-direction. On the other hand, in WSM, the surface states corresponding to Fermi arc[14] appear on surfaces normal to x-direction. Hence, large amplitudes are expected along z sides after integration along y. Owing to the presence of bulk Weyl node (shown as dilute dots) near the same energy $E = 0$, the right and left surfaces states are coupled and the high amplitude regions appear on both right and left sides.

We set $\beta = 0.4$ and varied $W \in [2.5, 4.5]$ to teach the features of DM, and $W \in [0.4, 1.6]$ to teach those of CI. For WSM, we set $\beta = 0.55$ and varied $W \in [0.3, 1.5]$. For DM and WSM, we have prepared 3000 samples for training the features of eigenfunctions, while 4000 samples have been prepared to teach the features of CI. We then varied β and W and let the machine calculate the probabilities $P_{\rm CI}, P_{\rm WSM}$, and $P_{\rm DM}(= 1 - P_{\rm CI} - P_{\rm WSM})$ that a given eigenfunction belongs to CI, WSM, and DM, respectively. We then draw a color map in the W-β plane as shown in Fig. 5, which qualitatively reproduces the phase diagram obtained by the transfer matrix method.[16]

4. Summary and Concluding Remarks

In this paper, we have considered three examples of 3D quantum phase transitions: the Anderson transition, transitions in topological insulators, and transitions in Weyl semimetal. From the universality class point of view, the Anderson transition belongs to the orthogonal class, while topological insulators belong to the symplectic class. Weyl semimetal realized by stacking Chern insulator belongs to the unitary class. We therefore have covered all the three Wigner-Dyson classes.[8–10] Applications of this method to other 7 non-standard universality classes with chiral and/or particle-hole symmetries[11,12] would be interesting.

By the machine learning, we could derive the approximate phase diagrams. In particular, the shift of phase boundaries between insulators with different topology as we increase disorder strength W has been captured. It should be emphasized that phase diagrams of topological insulators and Weyl semimetals have been determined by the results of learning along a finite one-dimensional lines in two-dimensional parameter space [see, for example, the arrows of Fig. 3 (a)].

The phase boundaries between DM and insulating phases such as OI, STI and WTI, on the other hand, are not as sharply determined as those of insulating phases with different topology. One possible reason is that the fluctuation of wave function amplitude in DM phase is much

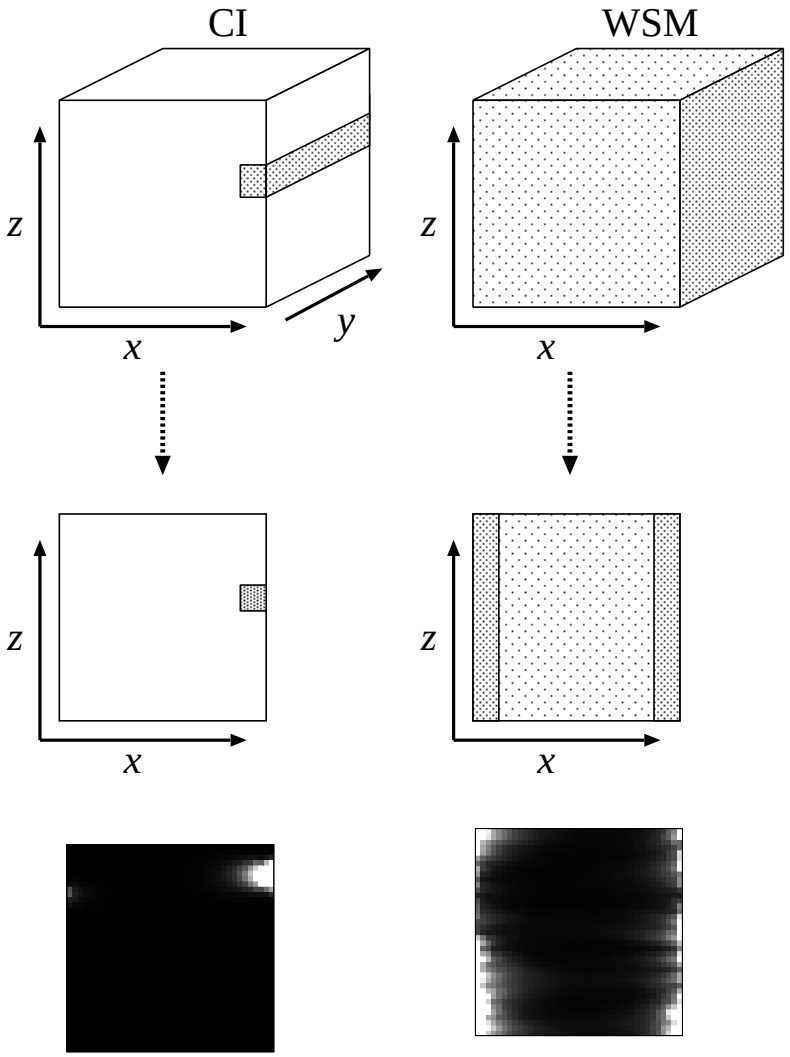

Fig. 4. Schematic of amplitudes and the results of integration over y coordinate of numerically calculated eigenfunctions (bottom panels). Periodic boundary condition is imposed in y- and z-directions, and fixed boundary condition in x. In the bottom panels, the modulus squared of a numerically obtained eigenfunction integrated over y is shown. (β, W)=(0.4, 0.6) (CI, bottom left) and (β, W)=(0.55, 0.9) (WSM, bottom right).

larger than that of the topological surface states. Significant fluctuation of wave function also arises in the case of WSM phase, where bulk wave functions near the Weyl nodes and surface states forming the Fermi arc are coupled. This might be the reason why the phase boundary between CI and WSM is obscurer than those of OI/STI, STI/WTI, and WTI(001)/WTI(111).

In some systems, transfer matrix approach is not applicable. In this paper, we have demonstrated [Fig. 3(b)] that the deep learning method proposed here can be applied to systems where the transfer matrix is not defined. Other applications to complicated lattices such as

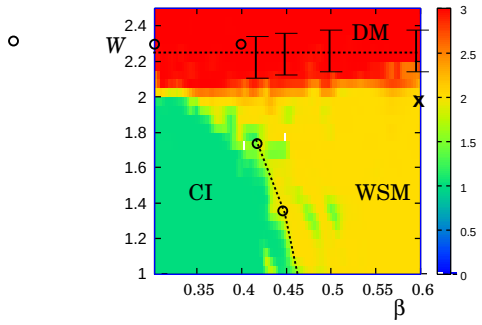

Fig. 5. Color map of $P_{\mathrm{CI}}, P_{\mathrm{WSM}}$, and P_{DM}. The intensity $1 \times P_{\mathrm{CI}} + 2 \times P_{\mathrm{WSM}} + 3 \times P_{\mathrm{DM}}$ is plotted. Bars with errors and circles (○) indicate the transfer matrix estimate of the critical points,[16] and dotted lines are guide to the eye. Cross (×) at $(\beta, W) \approx (0.6, 2.0)$ indicates the WSM/DM phase boundary estimated by the scaling of density of states.[16,42]

quantum percolation[46–49] and fractal lattice[50] are important future topics.

For the analysis of Anderson transition, we have used the known value of critical disorder W_c for training CNN. Natural question arises whether we can determine the critical disorder $W_c \approx 16.54$ by the current method instead of relying on other methods. One possibility for detecting the critical disorder might be to prepare the Fourier transformed wave functions. After Fourier transformation, localized states become delocalized in k-space while delocalized ones become localized. This duality is broken if we estimate W_c wrong. Careful monitoring of validation error of CNN for real-space and k-space wave functions would enable us to detect the wrong choice of W_c.

Machine learning has recently been applied to several problems of condensed matter physics such as Ising and spin ice models,[51,52] 2D topological system,[53] and strongly correlated systems.[54–59] Applications to interacting electron systems with disorder such as Anderson-Hubbard model[60,61] as well as topological systems of dirty boson such as quantum magnon Hall insulator[62] and topological photonic insulator[63] are interesting problems to be studied.

Acknowledgments

The authors would like to thank Koji Kobayashi for useful comments and for showing us a phase diagram corresponding to Fig. 3(a) obtained via the transfer matrix method prior to publication. Tomi Ohtsuki thanks Keith Slevin, Ken-Ichiro Imura, Shang Liu and Ryuichi Shindou for fruitful collaborations on 3D random electron systems treated in this paper. This work was partly supported by JSPS KAKENHI Grant No. JP15H03700.

Appendix

In the main text, we have plotted $0 \times P_{\mathrm{OI}} + 1 \times P_{\mathrm{W001}} + 2 \times P_{\mathrm{SW111}} + 3 \times P_{\mathrm{DM}}$, which is a convenient way to see various phases in single figure. Around the phase boundaries where P_i (i = OI, W001, SW111, DM) deviates from 0 or 1, however, this quantity becomes ambiguous. In this Appendix, we show each P_i to complement the plot in the main text, taking the case of Fig. 3 (a) as an example. From Fig. 6 (b), we see that no WTI(001) phase appears near the OI/STI boundary, so the green region near OI/STI boundary in Fig. 3 (a) is not WTI(001) phase, but is a transient region towards metal (Dirac semimetal, to be precise) phase, which appears on the phase boundary [see Fig. 6's panels (a) and (d)].

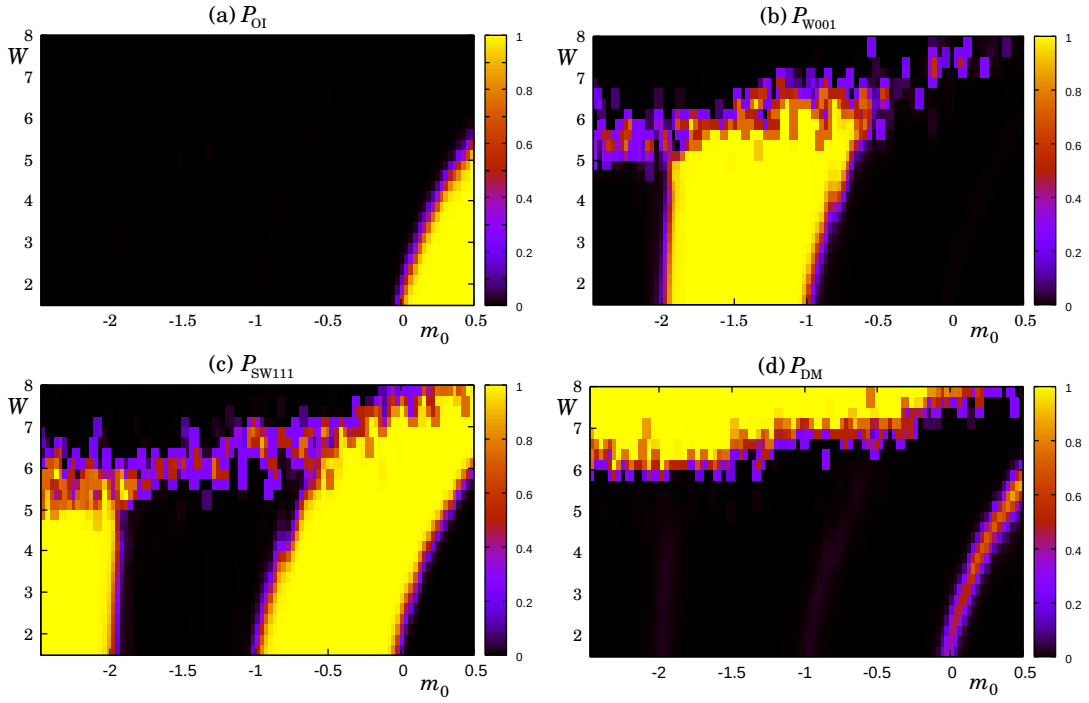

Fig. 6. Map view of P_i (i = OI, W001, SW111, DM) corresponding to Fig. 3 (a). (a) OI, (b) WTI(001), (c) STI/WTI(111), and (d) DM.

References

1) P. W. Anderson: Phys. Rev. **109** (1958) 1492.
2) M. Z. Hasan and C. L. Kane: Reviews of Modern Physics **82** (2010) 3045.
3) X.-L. Qi and S.-C. Zhang: Rev. Mod. Phys. **83** (2011) 1057.
4) S. Murakami: New Journal of Physics **9** (2007) 356.
5) A. A. Burkov and L. Balents: Phys. Rev. Lett. **107** (2011) 127205.
6) A. P. Schnyder, S. Ryu, A. Furusaki, and A. W. W. Ludwig: Phys. Rev. B **78** (2008) 195125.
7) A. Kitaev: AIP Conference Proceedings **1134** (2009) 22.
8) E. P. Wigner: The Annals of Mathematics **53** (1951) 36.
9) F. J. Dyson: Journal of Mathematical Physics **3** (1962) 140.
10) F. J. Dyson: Journal of Mathematical Physics **3** (1962) 1199.
11) M. R. Zirnbauer: Journal of Mathematical Physics **37** (1996) 4986.
12) A. Altland and M. R. Zirnbauer: Phys. Rev. B **55** (1997) 1142.
13) L. Fu and C. L. Kane: Phys. Rev. B **76** (2007) 045302.
14) R. Okugawa and S. Murakami: Phys. Rev. B **89** (2014) 235315.
15) C.-Z. Chen, J. Song, H. Jiang, Q.-f. Sun, Z. Wang, and X. C. Xie: Phys. Rev. Lett. **115** (2015) 246603.
16) S. Liu, T. Ohtsuki, and R. Shindou: Phys. Rev. Lett. **116** (2016) 066401.
17) B. Sbierski and P. W. Brouwer: Physical Review B **89** (2014) 155311.
18) H. Katsura and T. Koma: J. Math. Phys. **57** (2016) 021903.
19) H. Katsura and T. Koma: arXiv:1611.01928 (2016).
20) T. Ohtsuki and T. Ohtsuki: Journal of the Physical Society of Japan **85** (2016) 123706.
21) T. Obuchi, H. Koma, and M. Yasuda: Journal of the Physical Society of Japan **85** (2016) 114803.
22) Y. LeCun, Y. Bengio, and G. Hinton: Nature **521** (2015) 436.
23) D. Silver *et al.*: Nature **529** (2016) 484.
24) Y. Asada, K. Slevin, and T. Ohtsuki: Phys. Rev. Lett. **89** (2002) 256601.
25) J. P. Dahlhaus, J. M. Edge, J. Tworzydło, and C. W. J. Beenakker: Phys. Rev. B **84** (2011) 115133.

26) S. Ryu and K. Nomura: Phys. Rev. B **85** (2012) 155138.

27) K. Kobayashi, T. Ohtsuki, and K.-I. Imura: Physical Review Letters **110** (2013) 236803.

28) Y. LeCun, L. Bottou, Y. Bengio, and P. Haffner: Proceedings of the IEEE **86** (1998) 2278.

29) Y. Jia, E. Shelhamer, J. Donahue, S. Karayev, J. Long, R. Girshick, S. Guadarrama, and T. Darrell: arXiv:1408.5093 (2014).

30) X. Glorot and Y. Bengio: Aistats **9** (2010) 249.

31) T. Tieleman and G. Hinton: COURSERA: Neural Networks for Machine Learning **4** (2012) Lecture 6.5.

32) K. Slevin and T. Ohtsuki: New Journal of Physics **16** (2014) 015012.

33) A. Rodriguez, L. J. Vasquez, K. Slevin, and R. A. Romer: Phys. Rev. Lett. **105** (2010) 046403.

34) A. Rodriguez, L. J. Vasquez, K. Slevin, and R. A. Romer: Phys. Rev. B **84** (2011) 134209.

35) C.-X. Liu, X.-L. Qi, H. Zhang, X. Dai, Z. Fang, and S.-C. Zhang: Phys. Rev. B **82** (2010) 045122.

36) K.-I. Imura, M. Okamoto, Y. Yoshimura, Y. Takane, and T. Ohtsuki: Phys. Rev. B **86** (2012) 245436.

37) K. Kobayashi, Y. Yoshimura, K.-I. Imura, and T. Ohtsuki: Phys. Rev. B **92** (2015) 235407.

38) J. Li, R.-L. Chu, J. K. Jain, and S.-Q. Shen: Phys. Rev. Lett. **102** (2009) 136806.

39) C. W. Groth, M. Wimmer, A. R. Akhmerov, J. Tworzydło, and C. W. J. Beenakker: Phys. Rev. Lett. **103** (2009) 196805.

40) H.-M. Guo, G. Rosenberg, G. Refael, and M. Franz: Phys. Rev. Lett. **105** (2010) 216601.

41) Koji Kobayashi, private communications.

42) K. Kobayashi, T. Ohtsuki, K.-I. Imura, and I. F. Herbut: Phys. Rev. Lett. **112** (2014) 016402.

43) C.-Z. Chang, W. Zhao, J. Li, J. K. Jain, C. Liu, J. S. Moodera, and M. H. W. Chan: Phys. Rev. Lett. **117** (2016) 126802.

44) Y. Yoshimura, W. Onishi, K. Kobayashi, T. Ohtsuki, and K.-I. Imura: Phys. Rev. B **94** (2016) 235414.

45) X.-L. Qi, T. L. Hughes, and S.-C. Zhang: Phyical Review B **78** (2008) 195424.

46) Y. Avishai and J. M. Luck: Phys. Rev. B **45** (1992) 1074.

47) R. Berkovits and Y. Avishai: Phys. Rev. B **53** (1996) R16125.

48) A. Kaneko and T. Ohtsuki: Journal of the Physical Society of Japan **68** (1999) 1488.

49) L. Ujfalusi and I. Varga: Phys. Rev. B **90** (2014) 174203.

50) Y. Asada, K. Slevin, and T. Ohtsuki: Phys. Rev. B **73** (2006) 041102.

51) J. Carrasquilla and R. G. Melko: arXiv:1605.01735 (2016).

52) A. Tanaka and A. Tomiya: arXiv:1609.09087 (2016).

53) Y. Zhang and E.-A. Kim: arXiv:1611.01518 (2016).

54) G. Carleo and M. Troyer: arXiv:1606.02318 (2016).

55) P. Broecker, J. Carrasquilla, R. G. Melko, and S. Trebst: arXiv:1608.07848 (2016).

56) K. Ch'ng, J. Carrasquilla, R. G. Mello, and E. Khatami: arXiv:1609.02552 (2016).

57) L. Li, T. E. Baker, S. R. White, and K. Burke: Phys. Rev. B **94** (2016) 245129.

58) E. P. van Nieuwenburg, Y.-H. Liu, and S. D. Huber: arXiv:1610.02048 (2016).

59) L. Huang and L. Wang: Phys. Rev. B **95** (2017) 035105.

60) H. Shinaoka and M. Imada: Journal of the Physical Society of Japan **78** (2009) 094708.

61) Y. Harashima and K. Slevin: Phys. Rev. B **89** (2014) 205108.

62) B. Xu, T. Ohtsuki, and R. Shindou: Phys. Rev. B **94** (2016) 220403.

63) L.-H. Wu and X. Hu: Phys. Rev. Lett. **114** (2015) 223901.